Rydberg and autoionizing states of tellurium studied by laser resonance ionization spectroscopy

R. Li,[1,*] Y. Liu,[2] M. Mostamand,[1,3] T. Kieck,[4] K. D. A. Wendt,[4] and J. Lassen[1,3,5]

[1]*TRIUMF-Canada's Particle Accelerator Center, Vancouver, British Columbia, Canada V6T 2A3*

[2]*Physics Division, Oak Ridge National Laboratory, Oak Ridge, Tennessee 37831, USA*

[3]*Department of Physics and Astronomy, University of Manitoba, Winnipeg, Manitoba, Canada R3T 2N2*

[4]*Institute of Physics, Johannes Gutenberg University Mainz, D-55128 Mainz, Germany*

[5]*Department of Physics, Simon Fraser University, Burnaby, British Columbia, Canada V5A 1S6*

(Received 16 July 2019; published 22 November 2019)

Multistep laser-resonance-ionization spectroscopy of tellurium (Te) has been performed at TRIUMF's off-line laser ion source test stand. Six clean and regular even-parity Rydberg series $5p^3\ (^4S^\circ_{3/2})\ np\ ^3P_{0,1,2}$, $np\ ^5P_{1,2}$, and $nf\ ^3F_2/^5F_{1,2}$ were observed. The ionization potential of Te was extracted from the measured series as $72669.114(56)_{\rm stat}(45)_{\rm sys}$ cm^{-1}. Excited from two different intermediate levels, seven odd-parity autoionization Rydberg series converging to the $5s^25p^3\ (^2D^\circ_{3/2})$ core state of Te were obtained.

DOI: 10.1103/PhysRevA.100.052510

I. INTRODUCTION

Photoionization spectra of tellurium (Te) were first studied by Berkowitz *et al.* in 1981 by illuminating an atomic Te beam with monochromator-dispersed H and He light sources [1]. They obtained autoionization (AI) Rydberg series converging to $^2D^\circ_{3/2}$ $^2D^\circ_{5/2}$, $^2P^\circ_{1/2}$, and $^2P^\circ_{3/2}$ of the $5s^2\ 5p^3$ core configuration of Te. Shortly thereafter Mazzoni *et al.* used absorption spectroscopy to observe even-parity Rydberg series converging to the ionization potential (IP) of Te [2] and AI Rydberg series converging to the $^2D^\circ_{3/2}$ and $^2D^\circ_{5/2}$ ion core states [3]. Some of Berkowitz's AI series were reobserved in Mazzoni's spectra, but there were also disagreements. Chen *et al.* theoretically calculated the spectra of AI states of oxygen-group elements O, S, Se, and Te in 1994 [4]. Their result for S agreed well with experiments, but the calculation quality decreased significantly when going to the heavier atoms Se and Te, especially for Te.

With an open valence p shell, oxygen-group elements have rich electronic structures because of the interactions between several open shells and the presence of perturbing states in the midst of Rydberg series. As a heavy element in the oxygen group the Te ($Z = 52$) atom is expected to have not only strong correlations induced by the electrostatic interactions but also remarkable spin-orbit effects. The resulting complexity causes the difficulties in interpreting experimental spectra and the discrepancies between experiments and theoretical calculations [4]. More atomic spectroscopic data is needed to reveal the cryptic atomic properties, which can benefit theoretical atomic modeling [5], interpretation of astronomical spectra [6], and semiconductor technology [7].

Resonance ionization spectroscopy (RIS) has been applied to study atomic structures, especially high-lying Rydberg and AI states since the 1970s [8]. With its inherent element-selective ionization, RIS has become widely used at various accelerator facilities to deliver isobar-suppressed radioactive beams to nuclear physics experiments [9–12]. To develop optimal laser-ionization schemes, especially via highly efficient AI states, an off-line laser ion source test stand (LIS-STAND) dedicated to RIS was built at TRIUMF [13]. Various elements, Ga, Ca, Al, Sc, Cd, Y, Sb, and Lu, have already been studied using RIS at the LIS STAND [14–18].

Multistep resonance ionization of Te has been reported by Day Goodacre *et al.*, using a combination of Ti:sapphire (Ti:Sa) and dye lasers [19,20]. We recently obtained multiresonance photoionization spectra of Te in the AI region excited using all Ti:Sa lasers at Oak Ridge National Laboratory (ORNL) [21]. In that work, we observed four AI Rydberg series of $5s^2\,5p^3(^2D^\circ_{3/2})\ ns$ and nd configurations and, based on the convergences of the series, revised the IP value of Te that was determined from the absorption spectra by Cantú *et al.* more than 30 years ago [2]. However, we were restricted to one ionization scheme due to the limitation that the second harmonics of the Ti:Sa lasers at ORNL could not be continuously scanned over wide ranges. The present work continued our investigation on Rydberg and AI states of Te at the TRIUMF LIS-STAND, where a newly developed automated frequency-doubling system is available. This system enabled us to access different excitation paths for RIS of Te. The results include an observation of even-parity bound Rydberg series converging to the IP of Te and odd-parity AI Rydberg series converging to the excited core state $5s^25p^3(^2D^\circ_{3/2})$ of Te.

II. EXPERIMENTAL SETUP

The experimental setup is schematically shown in Fig. 1. Three Ti:Sa lasers, one grating tuned and two birefringent-filter (BRF) tuned, were simultaneously pumped by a single pulsed Nd:YAG laser with 30 W at 532 nm and 10 kHz pulse repetition rate. These Ti:Sa lasers provided output powers of 1–2.5 W in fundamental wavelengths (690–990 nm) with linewidth in the range of 1–10 GHz dependent on the laser

*ruohong@triumf.ca

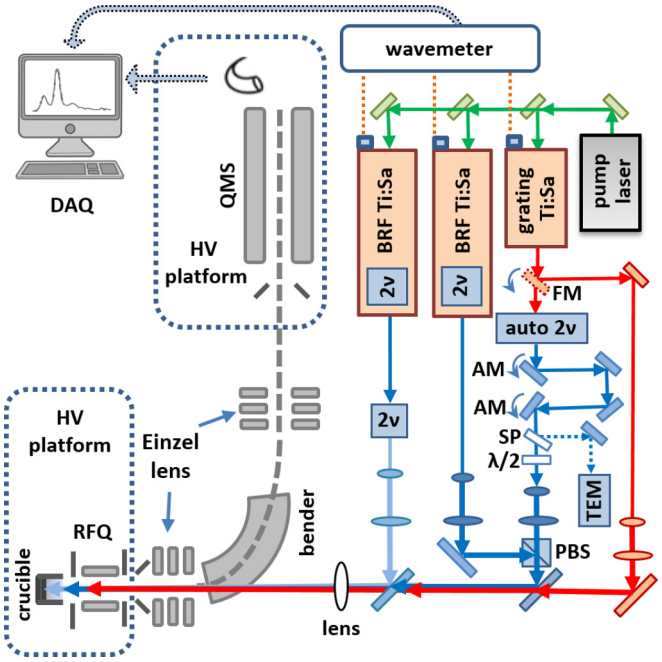

FIG. 1. Schematic setup for Te laser-ionization spectroscopy. Details of intracavity and external doubling are omitted for clarity. DAQ: data acquisition system; QMS: quadrupole mass spectrometer; RFQ: radio frequency quadrupole; FM: foldable mirror; AM: automated mirror; SP: beam sampler; PBS: polarization beam splitter; TEM: TEM BeamLock detectors.

optics, power, and wavelength. The laser pulse width was typically ~50 ns. To access the UV and blue excitation transitions of Te atoms (Fig. 2), frequency conversions via nonlinear crystals were employed. For two BRF-tuned lasers the frequency doubling was implemented inside the laser cavities for simple setup and good conversion efficiency [22]. The reflectivity of the output coupler was chosen deliberately to confine the fundamental (FD) emission inside the cavity and transmit the second harmonics (SH) out. The typical SH laser power was 200–500 mW. To generate the 214 nm laser light for Te excitation from the ground state to the intermediate level $5p^3(^3D^\circ_{3/2})6s\ ^3S^\circ_1$, a BBO crystal was used to further frequency double a SH laser. The obtained power was 11 mW at 214 nm.

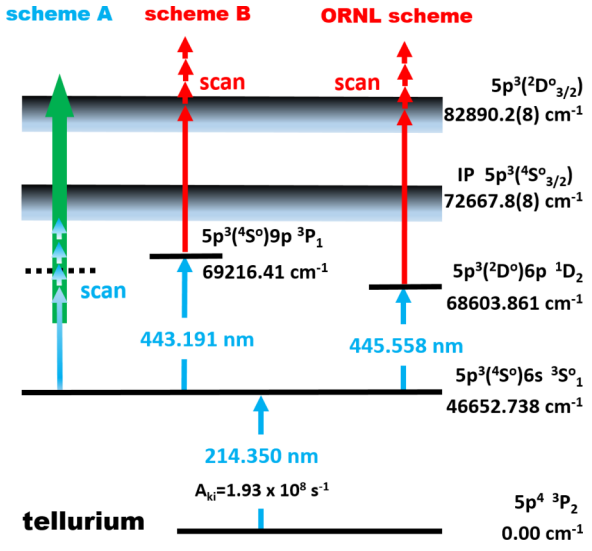

FIG. 2. Te excitation paths. Vacuum wavelengths are used. For the intermediate level of scheme B, the configuration $5p^3(^4S^o)9p\ ^3P_0$ and level energy 69216.413 cm^{-1} are from this experiment; for the intermediate level of ORNL scheme, the configuration $5p^3(^2D^o)6p\ ^1D_2$ and level energy 68603.861 cm^{-1} are from NIST ADS [27]; the IP value is from NIST ADS.

The grating-tuned Ti:Sa laser was designed for spectroscopy studies [23,24]. Its wavelength can be scanned continuously from 700 to 930 nm. Controlled by a 45° foldable mirror, the laser output can be either used directly at FD wavelengths or frequency doubled by a LBO crystal. To avoid time-consuming readjustments during wide wavelength scans, the crystal was mounted on an automated rotary stage with encoder. During scans, the crystal's optical axis was automatically rotated relative to the incident laser according to a grating-angle versus crystal-angle calibration. This automated system could achieve 80%–90% of the SH power available under manual adjustments. Due to the 8 mm length of the crystal, the walkoff of the laser beam in wide-wavelength scans had to be compensated in order to maintain proper spatial overlap of the laser beams in the ionization region. A commercial BeamLock 4D system from TEM Messtechnik was employed as a solution. As shown in Fig. 1, the laser path was readjusted by two automated mirrors (displacement and angle controls) after the doubling crystal, based on the images of a laser pickup on two TEM position sensitive detectors (monitoring near field and far field, respectively). To provide satisfactory precision in focusing the laser beams over a distance of about 8 m into the 3 mm diameter crucible, the distance of two TEM automated mirrors was extended to 60 cm.

All laser beams were expanded three to four times by telescope-type beam expanders before being spatially overlapped with each other via several 50 mm diameter dichroic mirrors. Two blue laser beams were combined with a polarizing beam splitter (PBS). The overlapped laser beams were focused by a single $f = 5$ m uncoated lens into a 3 mm diameter crucible inside the vacuum system where the Te sample was vaporized. The temporal superposition of the laser pulses was achieved with the help of intracavity Pockels cells. All laser wavelengths were measured by a wavemeter with a precision of 10^{-6} (HighFinesse WS/6). To ensure measurement accuracy, the wavemeter was routinely calibrated to a polarization stabilized HeNe laser with a wavelength accuracy of 10^{-8} (Melles Griot 05 STP 901/903).

Atomic absorption spectroscopy standard Te solution (Alfa Aesar Specpure, 1 g/l Te in 30% HNO_3 solution) was loaded into the crucible to generate Te atom vapor. The resistively heated crucible was operated at 1500 °C during the Te experiment to provide stable and consistent vaporization. After laser resonance ionization, the produced Te ions were guided by a radio frequency quadrupole (RFQ) to ion extraction and acceleration [25,26]. The accelerated ions were focused and sent to the detection system, which consisted of deceleration ion optics, quadrupole mass spectrometer (QMS, Extrel MAX-300), and a channel electron multiplier.

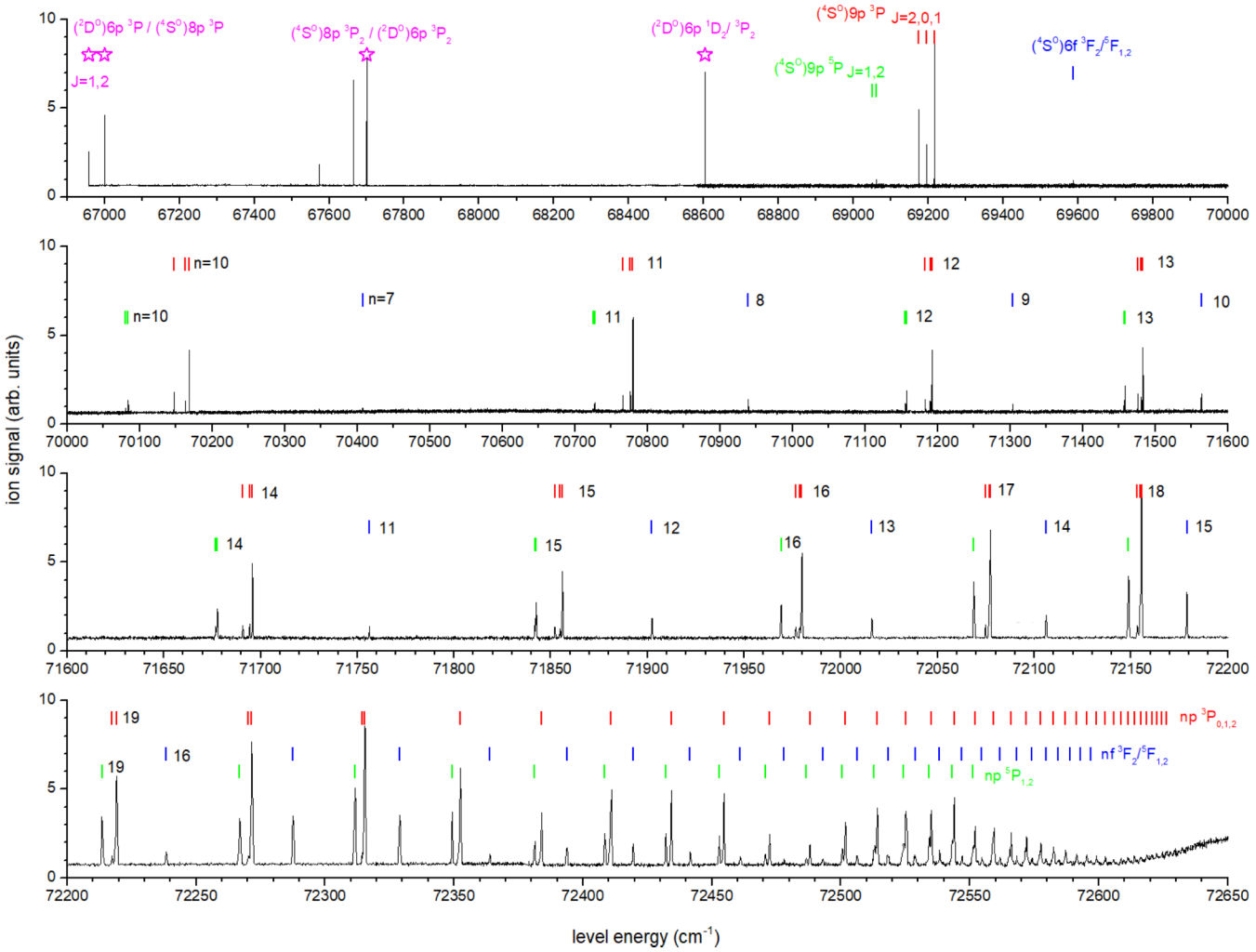

FIG. 3. Te even-parity Rydberg spectrum excited from the level of $5p^3(^4S^\circ_{3/2})6s\ ^3S_1$ 46652.738 cm^{-1}. The assigned levels are labeled with "|" and their principal quantum number n. Different series $5p^3(^4S^\circ_{3/2})np\ ^3P_{0,1,2}$, $5p^3(^4S^\circ_{3/2})np\ ^5P_{1,2}$, and $5p^3\ (^4S^\circ_{3/2})nf\ ^3F_2/^5F_{1,2}$ are colored as red, green, and blue, respectively, which matches with Fig. 4. The J values of fine-structure sublevels are marked out in the top subplot. The observed levels that coincide with NIST data are labeled with "☆" and their assigned configurations are from the NIST database [27]. The spectrum is composed of three individual scans: 67000–68610 cm^{-1}, 68000–71350 cm^{-1}, and 71300–72850 cm^{-1}. The scans were normalized via resonance peaks in the overlapping scan ranges. The laser power variation across the wide energy range (from ~30 mW at the low-energy to ~200 mW at the high-energy side) may affect the relative resonance peak heights.

III. EXPERIMENTAL PROCEDURE AND SPECTROSCOPY RESULTS FOR Te

To investigate both Rydberg states converging to the ionization potential (IP) $5p^3(^4S^\circ_{3/2})$ and autoionizing (AI) Rydberg states converging to the excited core state $5p^3(^2D^\circ_{3/2})$, different excitation and ionization schemes were chosen as shown in Fig. 2. The ionization region is defined by the 3 mm inside diameter of the crucible. The laser beams are prealigned and focused via the f = 5 m lens to a spot size of ~1 mm diameter inside the crucible. During the experiment, the beam foci were further optimized for best ion signals. The first excitation transition (214.350 nm_{vac}) was the same for all the schemes. This strong transition (A_{ki} = 1.93 × 10^8 s^{-1}) was found to be easily saturated with 7 mW input laser power, while the available power was typically ~11 mW. Scheme A aimed to study the even-parity Rydberg states at energies below the IP. The grating-tuned Ti:Sa laser with the automated frequency-doubling system was employed to provide tunable SH radiation in the range 385–493 nm for the second excitation from 46652.738 cm^{-1}. Subsequent nonresonant ionization was accomplished by a Nd:YVO_4 laser at 532 nm (Spectra-Physics YHP-40 Navigator II). Scheme B was designed to investigate the AI Rydberg states approaching the lowest excited core state $5p^3(^2D^\circ_{3/2})$ of Te. For this purpose, two excitation schemes were studied. The first used an intermediate state at 69216.41 cm^{-1} as the upper level of the second excitation step, which was found in the study with Scheme A. The second was the same scheme used in our previous work at ORNL [21]. It was remeasured here for comparison. For both schemes, a third laser with the FD radiation in the final step excited the valence electron to energies above IP, where the AI Rydberg levels were expected.

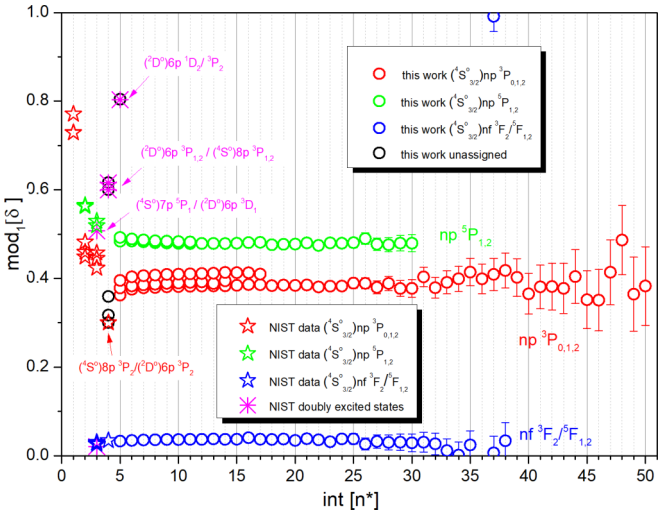

FIG. 4. Fano-Lu plot for the even-parity Rydberg series below the IP. The x axis is the integer part of the effective quantum number n^*. The y axis shows the decimal part of the quantum defect δ which mathematically expresses as $\mathrm{mod}_1[\delta]$. For np series, $n = \mathrm{int}[n^*] + 3$; for nf series, $n = \mathrm{int}[n^*]$. For clarity the fine-structure sublevels of $np\ ^3P_{0,1,2}$ series are marked in a same color "red", although distinguishable at low n. Likewise the sublevels of $np\ ^5P_{1,2}$ are all in "green". The J values of the $np\ ^3P_{0,1,2}$ splittings are 2, 0, and 1 from high to low δ, respectively; for $np\ ^5P_{1,2}$ the J values are 1, 2 from high to low δ, respectively. Different symbols are used for our data and NIST data, but the same color for the same series.

A. Rydberg spectrum via scheme A

Via scheme A three Rydberg series were obtained with very clear regularity. The detailed spectrum is shown in Fig. 3. The spectrum was taken at a resolution of ~2 GHz per step. The statistical error is estimated to be 0.15 cm^{-1} as determined by scanning multiple times on the resonance peaks at different wavelength regions as well as at different days. Furthermore, the scans were performed in both increasing and decreasing wavelength directions to include the uncertainties caused by the data acquisition (DAQ) delay. Therefore, the error takes into account the drifts of the first excitation laser frequency and the wavemeter performance.

Six Rydberg series of even parity are identified, as plotted in a Fano-Lu plot (Fig. 4) and compared with the NIST data [27]. From the intermediate level $5p^3(^4S^\circ)6s\ ^3S^\circ_1$, the possible Rydberg states excited by electric dipole transitions are $5p^3(^4S^\circ_{3/2})np\ ^3P_{0,1,2}$, $5p^3(^4S^\circ_{3/2})np\ ^5P_{1,2}$, and $5p^3(^4S^\circ_{3/2})nf\ ^3F_2/^5F_{1,2}$. To properly group and assign the observed Rydberg states, the Fano-Lu plot was drawn using the IP value of $72669.006(42)_{\mathrm{stat}}(20)_{\mathrm{sys}}$ cm^{-1} measured from our previous work at ORNL [21]. It shows that all Rydberg series have constant quantum defects at high-n numbers, instead of dramatically declining with n when using the old IP value 72667.8(8) cm^{-1} from Cantú *et al.* [2]. This corroborates the correctness of the ORNL value. The f shell valence electron has little interaction with the core due to the large angular momentum. From Fano's calculation for high-n Rydberg levels [28], the nf series of Te atom should have a quantum defect of around zero, which can be easily identified in the Fano-Lu plot. Similarly for the p shell valence electron at the energy close to the IP, the δ shall be around 3.5 for the Te atom.

With decreasing n, the np series start to split and show fine structures. These sublevel splittings gave a clear clue to distinguish the np Rydberg series $^3P_{0,1,2}$ and $^5P_{1,2}$. By comparing with listed values in the NIST database, the J values of different fine-structure sublevels are assigned as indicated in the top subplot of Fig. 3. The measured level energies are listed in Tables I–III. A few previously known members (n = 5–8) of these series [27] are also included in the tables, as well as in the Fano-Lu plot Fig. 4 for comparison. The state $5p^3(^4S^\circ_{3/2})9p\ ^3P_1$ was selected as the intermediate excitation state for scheme B. Several states could not be assigned in this work only based on the spectrum regularity, but they match with the reported states in the NIST database. These states are labeled by text in both Fig. 3 and Fig. 4. As shown in the spectrum and the Fano-Lu plot, the δ of the Rydberg series (including the NIST data for $\mathrm{int}[n^*]$ = 1–3) show constant quantum defects until $\mathrm{int}[n^*] < 10$. For all series the inner core fields start to influence in this low-n region. This normally causes a smooth deviation of δ, either positive or negative, asymptotically approaching the lowest n. Meanwhile, for $5p^3(^4S^\circ_{3/2})np$ series, the doubly excited states with the core state as $5p^3(^2D^\circ)6p$ perturb the series around n = 8 ($\mathrm{int}[n^*] = 4$ in Fig. 4). This causes a significant deviation of the δ of the np series locally in this region.

Our previous work [21] used AI Rydberg states to reevaluate the ionization potential for the Te atom, and refined the value from 72667.8(8) cm^{-1} to $72669.006(42)_{\mathrm{stat}}(20)_{\mathrm{sys}}$ cm^{-1}. Since the Rydberg spectrum obtained in this work has clearer series pattern and narrow linewidth resonances compared to the AI spectra, the IP value was remeasured using this spectrum. The Rydberg-Ritz formula expresses how the level energies of a Rydberg series converge to the IP:

$$E_n = V_{\mathrm{ion}} - \frac{R_M}{n^*} = V_{\mathrm{ion}} - \frac{R_M}{[n - \delta_l(n)]^2}. \quad (1)$$

Here E_n is the level energy, V_{ion} is the ionization potential, and R_M is the mass-reduced Rydberg constant for Te. The quantum defect $\delta_l(n)$ is dependent on both the principal quantum number n and the orbital angular momentum l. With increasing orbit angular momentum l, the valence electron has reduced interactions with the ionic core field and therefore has smaller δ_l, and vice versa. A good example is the $5p^3\ (^4S^\circ_{3/2})nf$ series in this work, which has $\delta_{l=3} \approx 0.03$, compared to $\delta_{l=1} \approx 3.4$ for $5p^3\ (^4S^\circ_{3/2})np$. For an l-specified unperturbed Rydberg series, $\delta_l(n)$ is only n dependent and can be expressed as the Ritz expansion:

$$\delta_l(n) = \delta_{l,0} + \frac{a_l}{(n - \delta_{l,0})^2} + \frac{b_l}{(n - \delta_{l,0})^4} + \cdots. \quad (2)$$

Here a_l and b_l are expansion constants dependent on l. For high-n numbers, the valence electron is far away from the ionic core and the Te atom becomes hydrogenlike; therefore, $\delta_l(n)$ is nearly constant at large n. When n gets lower, the interaction of the valence electron and the ionic core becomes

TABLE I. Te even-parity Rydberg series $5p^3\ (^4S^\circ_{3/2})np\ ^3P_{0,1,2}$ converging to the $V_{\rm ion}$ = 72669.1 cm^{-1}. The statistical error of the measured level energies in this work is 0.15 cm^{-1}. NIST data is displayed with its literature precision.

	J = 1			J = 0			J = 2		
n	This work σ(cm^{-1})	NIST σ(cm^{-1})	δ	This work σ(cm^{-1})	NIST σ(cm^{-1})	δ	This work σ(cm^{-1})	NIST σ(cm^{-1})	δ
5		4750.712	3.73		4706.495	3.73		0	3.77
6		55355.672	3.48		55809.132	3.45		55667.758	3.46
7		64088.997	3.42		63982.463	3.45		63921.485	3.46
8								67700.107	3.30
9	69216.41		3.36	69196.44		3.38	69175.21		3.40
10	70168.43		3.38	70162.72		3.38	70147.11		3.40
11	70779.79		3.38	70776.43		3.39	70766.07		3.41
12	71192.35		3.38	71189.87		3.39	71182.73		3.41
13	71483.03		3.38	71481.14		3.39	71476.12		3.41
14	71695.81		3.38	71694.33		3.39	71690.66		3.41
15	71856.06		3.38	71854.81		3.39	71852.13		3.41
16	71979.76		3.38	71978.74		3.39	71976.66		3.41
17	72077.27		3.38	72076.79		3.39	72074.75		3.41
18	72155.47		3.38	72154.68		3.39	72153.33		3.41
19	72219.08		3.38				72217.42		3.41
20	72271.53		3.39				72270.25		3.41
21	72315.40		3.39				72314.43		3.41
22	72352.46		3.38						
23	72383.88		3.38						
24	72410.90		3.38						
25	72434.22		3.39						
26	72454.61		3.38						
27	72472.36		3.38						
28	72488.02		3.38						
29	72501.79		3.39						
30	72514.14		3.39						
31	72525.25		3.38						
32	72535.05		3.39						
33	72544.04		3.38						
34	72552.08		3.38						
35	72559.18		3.40						
36	72565.98		3.38						
37	72571.95		3.39						
38	72577.44		3.40						
39	72582.44		3.41						
40	72587.18		3.40						
41	72591.44		3.41						
42	72595.38		3.42						
43	72599.11		3.40						
44	72602.64		3.37						
45	72605.75		3.38						
46	72608.68		3.38						
47	72611.43		3.38						
48	72613.92		3.40						
49	72616.44		3.35						
50	72618.67		3.35						
51	72620.64		3.41						
52	72622.47		3.49						
53	72624.56		3.36						
54	72626.27		3.38						

TABLE II. Te even-parity Rydberg series $5p^3\ (^4S^\circ_{3/2})nf\ ^3F_2/^5F_{1,2}$ converging to the $V_{\rm ion}$ = 72669.1 cm^{-1}. The data precision is the same as Table I.

	This work	NIST		
n	σ(cm^{-1})	σ(cm^{-1})	Term	δ
4		65703.814	$^5F_1$	0.03
4		65710.288	$^5F_2$	0.03
4		65719.741	$^3F_2$	0.03
5		68217.456	$^5F_2$	0.04
6	69587.05			0.03
7	70407.39			0.03
8	70939.19			0.04
9	71303.45			0.04
10	71563.64			0.04
11	71756.15			0.04
12	71902.31			0.04
13	72016.05			0.04
14	72106.17			0.04
15	72178.98			0.04
16	72238.45			0.04
17	72287.56			0.04
18	72329.00			0.04
19	72363.94			0.04
20	72393.72			0.04
21	72419.44			0.03
22	72441.58			0.04
23	72461.01			0.04
24	72478.08			0.03
25	72492.99			0.04
26	72506.29			0.04
27	72518.28			0.03
28	72528.81			0.03
29	72538.35			0.03
30	72546.92			0.03
31	72554.70			0.03
32	72561.73			0.03
33	72568.17			0.03
34	72574.11			0.01
35	72579.51			0.00
36	72584.31			0.02
37	72588.98			−0.01
38	72593.08			0.01
39	72596.83			0.03

non-negligible, which mathematically shows in Eq. (2) as the high-order terms become significant for small n. Two different effects take place: core penetration for low-l series and core polarization for high-l series. This expresses in Eq. (2) as a positive a when core penetration dominates and negative a when core polarization dominates. In Fig. 4, the δ of all np series shows an asymptotic increase at low-n numbers (including the NIST data for int$[n^*]$ = 1–3), except of a locally opposite trend of $np\ ^3P_{0,1,2}$ series at int$[n^*]$ = 4–10 caused by the perturbation from $5p^3(^2D^\circ)6p$. This implies the core penetration is the main contributor to the term defects for these series. Contrarily the nf series demonstrates a slow and smooth decrease at low-n numbers due to dominance of core polarization.

TABLE III. Te even-parity Rydberg series $5p^3\ (^4S^\circ_{3/2})np\ ^5P_{1,2}$ converging to the $V_{\rm ion}$ = 72669.1 cm^{-1}. The data precision is the same as Table I.

	J = 2			J = 1		
	This work	NIST		This work	NIST	
n	σ(cm^{-1})	σ(cm^{-1})	δ	σ(cm^{-1})	σ(cm^{-1})	δ
6		54199.122	3.56		54160.094	3.57
7		63610.819	3.52		63556.707	3.53
8						
9	69062.04		3.48	69051.04		3.49
10	70084.18		3.48	70080.42		3.49
11	70727.20		3.48	70725.01		3.49
12	71157.09		3.48	71155.57		3.49
13	71458.27		3.48	71457.18		3.48
14	71677.64		3.48	71676.92		3.48
15	71842.38		3.48	71841.84		3.48
16	71969.12		3.48			
17	72068.84		3.48			
18	72148.69		3.48			
19	72213.54		3.48			
20	72266.95		3.48			
21	72311.53		3.48			
22	72349.29		3.48			
23	72381.19		3.48			
24	72408.55		3.48			
25	72432.14		3.48			
26	72452.82		3.47			
27	72470.72		3.48			
28	72486.58		3.48			
29	72500.59		3.48			
30	72512.95		3.49			
31	72524.23		3.48			
32	72534.22		3.48			
33	72543.17		3.48			
34	72551.29		3.48			

Using the nonlinear least-squares routine, the IP and expansion constants were individually optimized for three series: $np\ ^5P_1$, $np\ ^3P_1$, and $nf\ ^3F_2/^5F_{1,2}$. Figure 5 shows the fitting curves and residuals with three Ritz expansion parameters $\delta_{l,0}$, a_l, and b_l. To avoid the strong perturbation around n = 8 and the growing core effect on the low-n members, the data fitting for both $np\ ^5P_1$ and $np\ ^3P_1$ series was started from n = 13. Different Ritz expansion orders were tested to estimate the uncertainty from fitting models. The data fitted well using different models (one, two, or three expansion orders) and all achieved an even distribution of the residuals around zero and within an individual level-energy uncertainty of 0.15 cm^{-1}. The extracted IP values via different models are shown in Fig. 6. The averaged IP values for individual series were 72669.066(21) cm^{-1} for $np\ ^5P_1$ series, 72669.100(24) cm^{-1} for $np\ ^3P_1$ series, and 72669.175(8) cm^{-1} for $nf\ ^3F_2/^5F_{1,2}$ series. The error bars were calculated as the standard deviation of the fitted values from different models. By averaging the results of the three series, the IP was determined as 72669.114(56) cm^{-1}. Considering the uncertainty from the intermediate state energy 46652.738(5) cm^{-1} [29] and

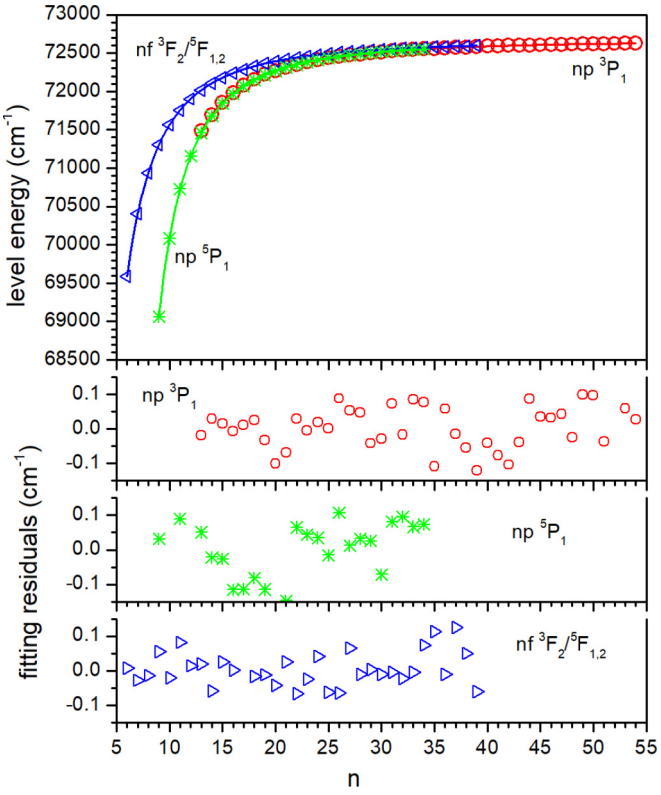

FIG. 5. Rydberg Ritz fits of the three series $np\ ^5P_1$, $np\ ^3P_1$, and $nf\ ^3F_2/^5F_{1,2}$.

systematic uncertainty 0.04 cm^{-1} [30] from the wavemeter, the IP is determined to be $72669.114(56)_{\text{stat}}(45)_{\text{sys}}$ cm^{-1}. This result agrees with the previously measured IP value at ORNL $72669.006(42)_{\text{stat}}(20)_{\text{sys}}$ cm^{-1} within the uncertainties. The numerical IP discrepancy may come from the systematic uncertainties between the different apparatuses and laser systems. Although both IP determinations used the method of resonance ionization spectroscopy, in the ORNL work autoionizing Rydberg states were used to extract the IP value, whereas in this work Rydberg series were used instead with different laser excitation schemes. Some hidden systematic uncertainty, such as the uncertainty from the fitting model of the autoionizing state Fano profiles as well as the uncertainty from the intermediate level energy, are possible.

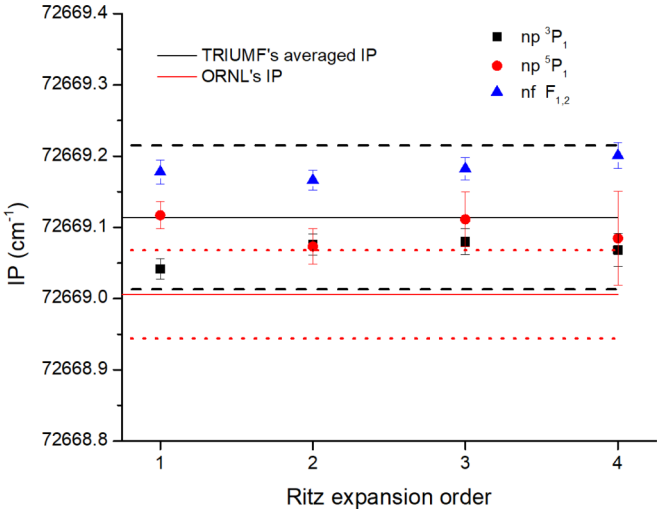

FIG. 6. Fitting model test with different Ritz expansion orders. TRIUMF's and ORNL's IP values are marked as solid straight lines in black and red, respectively. Their uncertainties, estimated as the sum of systematic and statistical uncertainties, are shown as the dashed line with the associated colors.

B. AI Rydberg spectrum via scheme B

AI Rydberg states were obtained via two three-step schemes, one utilizing the Rydberg state $5p^3(^4S^\circ_{3/2})9p\ ^3P_1$ at 69216.41(15) cm^{-1} observed in scheme A as the second intermediate state (scheme B in Fig. 2), and the other using the ORNL scheme [21], since it is excited from a different intermediate state $5p^3(^2D^\circ_{3/2})6p\ ^1D_2$ at 68603.861(5) cm^{-1} [29]. For both schemes, the wavelength of the grating-tuned Ti:Sa laser was scanned to obtain the AI Rydberg series converging to the excited core state $5p^3(^2D^\circ_{3/2})$. The ORNL spectrum was remeasured to check the possible systematic uncertainty. The obtained spectra are shown in Fig. 7. Unlike the narrow Rydberg resonances, some AI peaks have quite broad structures of tens or even hundreds cm^{-1} width due to strong interaction with the continuum. Scanning such extended resonance structures is demanding as the experimental conditions, e.g., laser intensities, laser pulse synchronization, spatial laser beam overlap in the ionization volume, etc., must be stable. To check the reproducibility and statistical uncertainty, both spectra have been scanned several times. An example of repeating scans is shown in Fig. 7.

Due to the interaction between the continuum and embedded discrete atomic states, AI states typically show Fano profiles [31], which can be described by considering two channels (the continuum and the AI series of interest):

$$I(\epsilon) = I_{res}\frac{(q+\epsilon)^2}{(1+\epsilon^2)} + I_{cont} \quad \text{with } \epsilon = \frac{E - E_{res}}{\Gamma/2}. \tag{3}$$

E_{res} is the resonance energy of the discrete state. Γ is the resonance width, e.g., the decay rate of the discrete state to the continuum (assuming the radiative decay probability is negligible), which is determined by the interaction strength between the discrete state and the continuum. For an unperturbed series, $n^{*3}\Gamma$ is a constant. I_{cont} is the nonresonant ionization signal excited from the intermediate level to the continuum. q is the Fano parameter, also called shape index. $\pi q^2/2$ presents the ratio of transition probabilities of two electron excitation paths: from the intermediate level to the discrete state and to the continuum in the resonance width Γ [31].

When $|q| \gg 1$ the excitation to the discrete state dominates; therefore, the profile is Lorentzian. When $|q| \sim 1$ the excitations through both paths are comparable and the profile is asymmetric. When $|q| \sim 0$ the excitation to the discrete state is much weaker than that into the continuum, which results in a window profile. Therefore, the shape of the AI resonance strongly depends on the intermediate level where the valence electron is excited from.

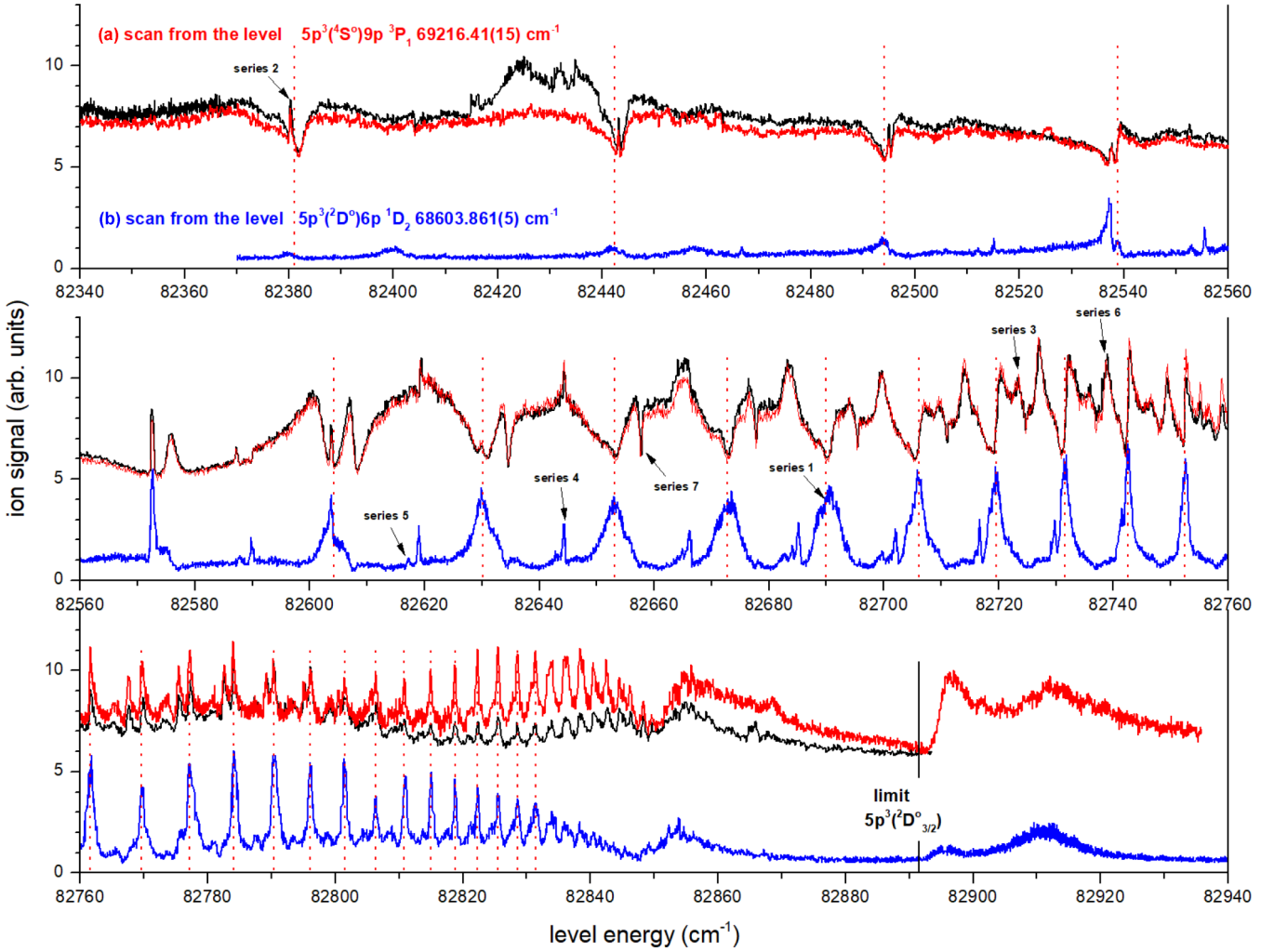

FIG. 7. AI Rydberg spectra excited from $5p^3(^4S^\circ_{3/2})9p\ ^3P_1$ 69216.41(15) cm^{-1} [spectrum (a)] and $5p^3(^2D^\circ_{3/2})6p\ ^1D_2$ 68603.861(5) cm^{-1} [spectrum (b)]. An example of repeating the scan (black line) was presented for spectrum (a). The ion signal is in arbitrary units (arb. units). For clearly displaying and comparing the spectra, spectrum (a) was shifted up by 2 arb. units. The most prominent AI series (series 1) was marked by red dotted lines to guide the eye to the evolution of the resonance shapes.

For the energy range investigated in this work, the adjacent ionization limit is $(^2D^\circ_{3/2})ns, nd$. The underlying continuum is $(^4S^\circ_{3/2})\varepsilon l$. The excitation from $5p^3(^4S^\circ_{3/2})9p$ [Fig. 7(a)] to the continuum is much more favored than that from $5p^3(^2D^\circ_{3/2})6p$ [Fig. 7(b)], since only single electron excitation is needed for the former. Similarly the excitation from $5p^3(^2D^\circ_{3/2})6p$ to the possible AI discrete states $(^2D^\circ_{3/2})ns, nd$ will be favored over that from $5p^3(^4S^\circ_{3/2})9p$. The corroborative evidence is the much higher baseline in spectrum (a) and Lorentzian profile for most resonance peaks in spectrum (b).

To study atomic structures, spectrum (b) is certainly preferred due to its simplicity, even though the most prominent AI series in spectrum (b) (series 1 in Fig. 7) slowly changes in shape from a Lorentzian to an asymmetric profile towards the low-energy end. It shows clearly that for the AI states in a same series q is not a constant, especially over a wide energy range. First, in the neighborhood of a perturbation, q certainly changes, and sometimes even switches the sign [32]. Even without perturbations, the excitation rates from the intermediate level to the final AI state and to the continuum vary. Typically the photoexcitation probability to the Rydberg states belonging to a series scales as $(n^*)^{-3}$ [33,34]. This effect is negligible at high-n end, but it becomes significant when approaching low-n values. It can explain the slow shape change of the AI resonances in spectrum (b). On the other hand, the excitation rate to the continuum is linearly dependent on the laser power. The energy range in Fig. 7 was accessed by scanning the grating-tuned Ti:Sa laser from 726 to 700 nm for spectrum (b) and from 728 to 760 nm for spectrum (a). The laser power in both cases increased when scanning towards lower energy. When the photoexcitation cross section to the continuum is quite low, as in the case of spectrum (b), the effect of the laser power variation is diminished. In contrast, for spectrum (a) it is prominent: the AI resonance shape of series 1 changes from Lorentzian to asymmetric and then to window profile from high to low energy [the resonance line centers are indicated by dotted (red) lines in Fig. 7]. The decrease of the photoexcitation to the discrete AI states and the increase of the nonresonance ionization both contribute to this line-shape evolution. A similar laser power effect was

TABLE IV. AI series converging to the limit of $^2D^\circ_{3/2}$ 82891.505 cm^{-1}. The values are extracted from both spectrum (a) and spectrum (b) in Fig. 7. n is assigned according to Berkowitz's [1] and our previous work at ORNL [21], for ns series $n \sim n^* + 4$ and for nd series $n \sim n^* + 2.5$. All resonances were fitted by Gaussian profile except those specifically noted. Series 7 signals were too small to fit properly in spectrum (b), but were measured at ORNL [21] using the same excitation scheme.

	σ (cm^{-1})												
	Series 1						Series 4		Series 5			Series 7	
	(Series III in [21])		Series 2		Series 3		(Series II in [21])		(Series I in [21])		Series 6	(Series IV in [21])	
	$nd_{3/2}$		$nd_{5/2}$		$nd_{3/2}$		$ns_{1/2}$		$ns_{1/2}$		$nd_{3/2}$	$nd_{5/2}$	
n	$J = 1, 2$		$J = 1, 2$		$J = 1, 2$		$J = 1, 2$		$J = 1, 2$		$J = 0$	$J = 1, 2$	
	(a)	(b)	(a)	(b)	(a)	(b)	(a)	(b)	(a)	(b)	(a)	(a)	ORNL[b]
17	82380.04	82380.04[a]		82380.33									82379.80
18	82444.11	82441.75[a]		82443.20									82443.27
19	82494.16	82494.34[a]		82494.97									82495.61
20	82538.84	82538.09[a]	82537.52	82537.68				82466.81					82539.13
21		82575.72[a]	82572.59	82572.54	82575.94			82515.10		82511.98			82576.11
22	82604.24	82603.53	82603.63		82606.73		82555.65[a]	82555.53	82552.58	82552.96			82607.35
23	82630.18	82630.09	82629.99		82633.25		82590.04[a]	82589.91	82587.18	82587.84		82634.69	82634.38
24	82653.08	82653.01			82656.57		82619.11[a]	82619.04	82617.03	82617.22		82657.64	
25	82672.73	82672.87			82676.55		82644.32	82644.27		82642.96	82664.97	82677.73	82677.74
26	82689.99	82690.49			82693.92			82666.08		82664.92	82683.41	82695.40	82695.38
27	82706.15[a]	82705.95			82709.64			82685.10		82684.04	82699.61	82710.95	82710.96
28	82719.65[a]	82719.56			82723.29			82702.00			82714.14	82724.76	82724.70
29	82731.52[a]	82731.70			82735.72			82716.72		82716.14	82727.13	82736.98	82737.07
30	82742.55[a]	82742.57			82746.14			82729.75			82738.89	82748.01	82747.94
31	82752.45[a]	82752.51			82756.49			82741.53			82749.46		
32	82761.56[a]	82761.65			82765.21	82765.68					82759.04		
33	82769.67[a]	82769.74			82773.30	82773.74					82767.68		82774.60
34	82777.14[a]	82777.38			82780.96	82780.86					82775.67		82781.84
35	82784.02	82784.21			82787.61					82789.22			
36	82790.34	82790.53			82793.30	82793.70					82795.23		
37	82796.12	82796.09			82799.26	82798.83					82800.60		82800.12
38	82801.47	82801.53			82804.15	82804.70					82805.66		82805.08
39	82806.33	82806.31			82809.14	82808.61					82810.24		
40	82810.84	82810.98			82813.48	82813.80							
41	82814.96	82815.03			82817.60	82817.72							
42	82818.77	82818.81			82821.10	82821.26							82821.64
43	82822.25	82822.34			82824.91	82824.50							
44	82825.48	82825.57			82827.91	82827.75							
45	82828.54	82828.59			82830.80								
46	82831.36	82831.45											

[a]Fitted with Fano profile.
[b]Data from our previous work at ORNL [21].

observed by Afrousheha [35] on AI states of Ba. All of these complexities intensify the difficulty in assigning the AI states as well as determining their line centers.

An advantage of this work compared to our previous work at ORNL is the observation of an additional spectrum excited from a different intermediate level. Comparing the two spectra gives a good overview of the resonance line-shape evolution, and helps to assign the series and to choose the proper profile formula in fitting the resonances. Seven and five AI Rydberg series were observed in spectra (a) and (b), respectively, all converging to the first excited state $^2D^\circ_{3/2}$ of the Te ion core. The results are presented in Table IV and plotted in a Fano-Lu plot (Fig. 8). Excited from two intermediate levels, the following electric-dipole-allowed Rydberg series are expected:

$$a): \quad 5p^3(^4S^\circ)9p\,^3P_1 \rightarrow 5p^3(^2D^\circ_{3/2}) \qquad ns_{1/2}, J = 1, 2,\ nd_{3/2}, J = 0, 1, 2,\ nd_{5/2}, J = 1, 2,$$

$$b): \quad 5p^3(^2D^\circ)6p\,^1D_2 \rightarrow 5p^3(^2D^\circ_{3/2}) \qquad ns_{1/2}, J = 1, 2,\ nd_{3/2}, J = 1, 2,\ nd_{5/2}, J = 1, 2, 3.$$

The assignment has been based on the jj coupling between the total angular momentum of the ion core j_c and the orbital angular momentum of the valence electron j_e. For heavy elements like Te significant spin-orbit interactions break down

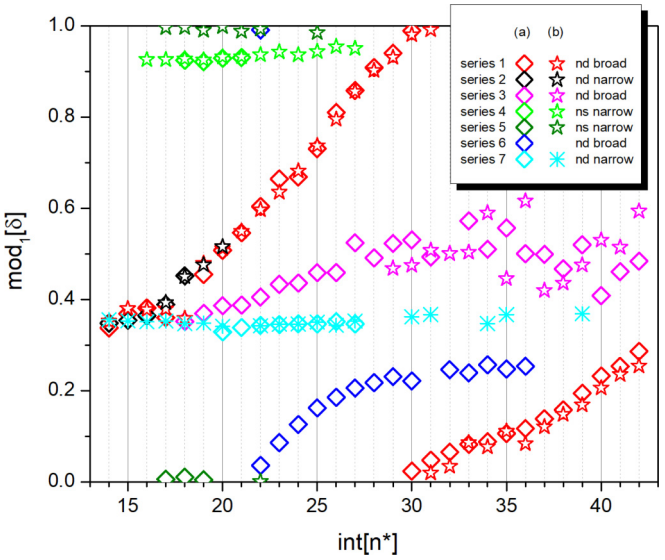

FIG. 8. Fano-Lu plot for the obtained AI states. Different series use different colors. All observed levels are symboled as ◇ for spectrum (a), ☆ for spectrum (b), and ∗ for series 7 measured in our previous work at ORNL using the same excitation scheme [21].

LS coupling, which manifests itself by the allowed transition from the triplet $6s\ ^3S^\circ_1$ to a singlet state $6p\ ^1D_2$. This transition was used as the second excitation step in the ORNL scheme (Fig. 2). In addition, at the high-n region investigated here ($n^* > 15$) the valence electron becomes decoupled from the ion core, which also leads the breakdown of *LS* coupling. Even for a light element like sulfur, *LS* coupling describes the low states well, but is not proper for the high-n states [36]. For jj coupling, the only good quantum number of the ion core is j_c. The $\mathrm{mod}_1[\delta]$ of *ns* and *nd* Rydberg electrons for oxygen-group elements regarding the ground state of the ion core $^4S^\circ_{3/2}$ are ~0.95 and ~0.4 [37]. This matches with the observed AI series converging to the first excited state of the ion core $^2D^\circ_{3/2}$ (Fig. 8). Based on the characteristic $\mathrm{mod}_1[\delta]$, disregarding the perturbation, the observed series can be clearly grouped into two *ns* and five *nd* series as shown in Table V.

The five *nd* series can be grouped based on their resonance width: series 1, 3, and 6 are broad, and series 2 and 7 are narrow. The three broad series were all observed in spectrum (a) but only two of them were observed in spectrum (b). This matches only with the configuration $nd_{3/2}$. Among these $nd_{3/2}$ series, series 6 was not observed in spectrum (b); thus it is assigned as $J = 0$. The other two series (series 1 and 3) were observed in both spectra (a) and (b), thus assigned as $J = 1$ or 2.

The two narrow *nd* series (series 2 and 7) are assigned as $nd_{5/2}$. The members of series 7 are visible in spectrum (b) as tiny window resonances beside the shoulders of series 1 peaks; however, due to the low signal-to-noise (S/N) ratio we could not extract their positions. Since in our previous work at ORNL series 7 was clearly observed and measured using the same scheme, we have listed the ORNL data for series 7 in Table IV. In addition, series 1 and series 2 shall have the same J, because of the same deviation of δ (Fig. 8) regarding the perturbation, and so do series 3 and 7.

AI Rydberg series 1, 4, 5, and 7 have been previously reported [1,3,21]. Series 1 is the most prominent broad resonance in spectrum (b), which is also observed in spectrum (a). The narrow series 4 and 5 were assigned as *ns* in previous works due to their characteristic δ values. Their narrow resonances and nearly constant δ make them ideal to extract the ionization limit in our previous work at ORNL, along with series 7. The previous works assigned series 1 and 7 as *nd* series only. With the spectroscopic data of this work, we were able to make more specific assignment of $nd_{3/2}$ and $nd_{5/2}$, and even determined J values for some series.

Three *nd* series were not observed in the ORNL work: series 2, 3, and 6. Series 2 is the sharp features sprouting on top of the broad peaks of series 1 in spectrum (b) and near the valley of the window resonances of series 1 in spectrum (a). Only four to five members of this series were identified. These sharp structures were overwhelmed by the intense broad peaks of series 1 in spectrum (a), which was the reason why we did not observe them in the previous work at ORNL. In spectrum (a) series 1 evolves from a Lorentz profile into a window resonance at low-energy range; as a consequence series 2 stood out prominently and enabled us to identify them. Series 3 and 6 are the broad peaks located between the intense broad peaks of series 1. They are the triples of a same configuration, which is evident in the energy range of 82720–82800 cm^{-1} in spectrum (a).

The differences of the level energies measured from spectra (a), (b) and our previous work at ORNL are shown in a histogram (Fig. 9). The differences between the measurements are drawn for three level sets: ΔE=spectrum (a)–ORNL, ΔE=spectrum (b)–ORNL, and ΔE=spectrum (a)–spectrum (b). The data statistics were quantitatively presented as "mean ± standard deviation" of ΔE in the figure. As shown in the comparison, there is no obvious systematic deviation between the measurements between spectra (a) and (b), as well as between spectra (a), (b), and ORNL. This indicates a good agreement between these two works. The standard deviations of ΔE distributions of three level sets are similar around 0.4 cm^{-1}, which shows the typical statistical uncertainty in measuring AI states of Te via our RIS method. The uncertainty of AI measurements is bigger compared to that of Rydberg states below the IP, due to the significant overlapping of the resonances and the complicated resonance shape variations.

TABLE V. Assignment of the series configurations and J values. Series 1 and series 2 shall have the same J, because of the same deviation of δ regarding the perturbation (see Fig. 8), and so do series 3 and 7.

Configuration	Series	J	$\mathrm{mod}_1[\delta]$	Figure
$(^2D^\circ_{3/2})nd_{3/2}$	1 3 6	1,2 0	~0.35	Broad
$(^2D^\circ_{3/2})nd_{5/2}$	2 7	1,2	~0.35	Narrow
$(^2D^\circ_{3/2})ns_{1/2}$	4 5	1,2	~0.95	Narrow

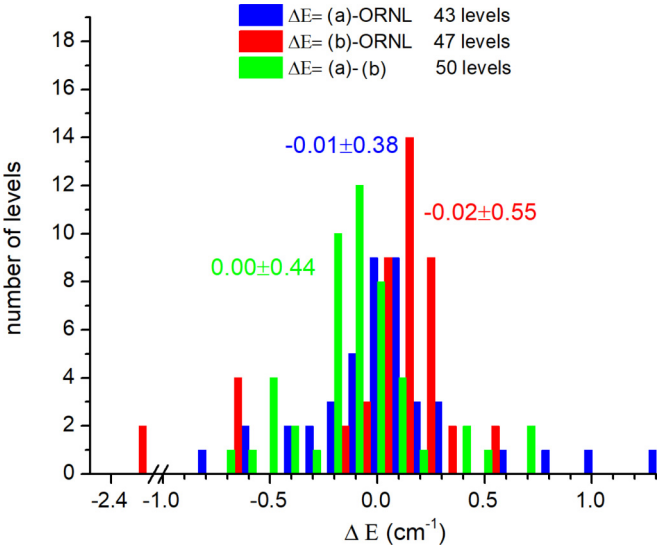

FIG. 9. Comparison of the level energies measured from spectra (a), (b) and our previous work at ORNL. ΔE was calculated as the differences between the measurements of each two spectra: spectrum (a)–ORNL, spectrum (b)–ORNL, and spectrum (a)–spectrum (b). The statistic of each data set is labeled nearby the peak as "mean ± standard deviation" of ΔE.

IV. CONCLUSION

Laser resonance ionization spectra of Te have been obtained at TRIUMF's offline laser ion source test stand. Six even-parity Rydberg series $5p^3np\ ^3P_{0,1,2}$, $5p^3np\ ^5P_{1,2}$, and $5p^3\ nf\ ^3F_2/^5F_{1,2}$ were observed converging to the IP $5p^3(^4S^\circ_{3/2})$. Using these measured Rydberg state energies, the IP value was extracted to be $72669.114(56)_{\rm stat}(45)_{\rm sys}$ cm^{-1}, which agrees with our previous measurement of $72669.006(42)_{\rm stat}(20)_{\rm sys}$ cm^{-1} at ORNL using AI Rydberg states. Furthermore, seven odd-parity AI Rydberg series converging to the excited core state $5p^3(^2D^\circ_{3/2})$ were measured via two different laser excitation paths. By comparison of the two spectra, excited from different intermediate states, the configurations of these series have been assigned and their J values are narrowed down. In addition, line-shape evolution in the AI states was observed and could be attributed to laser power dependence. These data will be useful to improve our understanding of the atomic structures of tellurium and develop efficient laser-ionization schemes for radioactive Te isotopes.

ACKNOWLEDGMENTS

The experimental work has been funded by TRIUMF which receives federal funding via a contribution agreement with the National Research Council of Canada and through a Natural Sciences and Engineering Research Council of Canada (NSERC) Discovery Grant (No. SAP-IN-2017-00039). Y.L. acknowledges support from the U.S. Department of Energy, Office of Science, Office of Nuclear Physics under Contract No. DE-AC05-00OR22725. M.M. acknowledges funding through the University of Manitoba graduate fellowship. T.K. acknowledges financial support from the DFG Research Unit FOR 2202 (ECHo) under Contract No. DU 1334/1-1.

[1] J. Berkowitz, C. H. Batson, and G. L. Goodman, Phys. Rev. A **24**, 149 (1981).
[2] A. M. Cantú, M. Mazzoni, and Y. N. Joshi, Phys. Scr. **84**, 261 (1983).
[3] M. Mazzoni, A. M. Cantú, and Y. N. Joshi, J. Phys. B: At. Mol. Phys. **16**, 3183 (1983).
[4] C.-T. Chen and F. Robicheaux, Phys. Rev. A **50**, 3968 (1994).
[5] M. Aymar, C. H. Greene, and E. Luc-Koenig, Rev. Mod. Phys. **68**, 1015 (1996).
[6] E. Anders and N. Grevesse, Geochim. Cosmochim. Acta **53**, 197 (1989).
[7] S. Hudgens and B. Johnson, Mater. Res. Soc. Bull. **29**, 829 (2004).
[8] R. Solarz, C. May, L. Carlson, E. Worden, S. Johnson, and J. Paisner, Phys. Rev. A **14**, 1129 (1976).
[9] J. Lassen, P. Bricault, M. Dombsky, J. P. Lavoie, Ch. Geppert, and K. Wendt, Hyperfine Interact. **162**, 69 (2005).
[10] V. N. Fedosseev *et al.*, Rev. Sci. Instrum. **83**, 02A903 (2012).
[11] I. D. Moore, A. Nieminen, J. Billowes, P. Campbell, Ch. Geppert, A. Jokinen, T. Kessler *et al.*, J. Phys. G **31**, S1499 (2005).
[12] R. Ferrer, V. T. Sonnenschein, B. Bastin, S. Franchoo, M. Huyse, Yu. Kudryavtsev, T. Kron *et al.*, Nucl. Instrum. Methods Phys. Res., B **291**, 29 (2012).
[13] J. P. Lavoie, R. Li, P. Bricault, J. Lassen, O. Chachkova, and A. Teigelhöfer, Rev. Sci. Instrum. **84**, 013306 (2013).
[14] R. Li, J. Lassen, A. Teigelhöfer, J. P. Lavoie, P. Bricault, O. Chackakova, J. Meissner, and Y. Zlateva, Nucl. Instrum. Methods Phys. Res., B **308**, 74 (2013).
[15] A. Teigelhöfer, J. Lassen, Z. Abboud, P. Bricault, H. Heggen, P. Kunz, R. Li, T. Quenzel, and S. Raeder, Hyperfine Interact. **216**, 65 (2013).
[16] S. Raeder, M. Dombsky, H. Heggen, J. Lassen, T. Quenzel, M. Sjödin, A. Teigelhöfer, and K. Wendt, Hyperfine Interact. **216**, 33 (2013).
[17] R. Li, J. Lassen, J. Ruczkowski, A. Teigelhöfer, and P. Bricault, Spectrochim. Acta Part B **128**, 36 (2017).
[18] R. Li, J. Lassen, Z. P. Zhong, F. D. Jia, M. Mostamand, X. K. Li, B. B. Reich, A. Teigelhöfer, and H. Yan, Phys. Rev. A **95**, 052501 (2017).
[19] T. Day Goodacre, D. Fedorov, V. N. Fedosseev, L. Forster, B. A. Marsh, R. E. Rossel, S. Rothe, and M. Veinhard, Nucl. Instrum. Methods A **830**, 510 (2016).
[20] T. Day Goodacre, J. Billowes, K. Chrysalidis, D. V. Fedorov, V. N. Fedosseev, B. A. Marsh, P. L. Molkanov, R. E. Rossel, S. Rothe, C. Seiffert, and K. D. A. Wendt, Hyperfine Interact. **238**, 4 (2017).

[21] T. Kieck, Y. Liu, D. W. Stracener, R. Li, J. Lassen, and K. D. A. Wendt, Spectrochim. Acta Part B **159**, 105645 (2019).
[22] J. Lassen, R. Li, S. Raeder, X. Zhao, T. Dekker, H. Heggen, P. Kunz, C. D. P. Levy, M. Mostanmand, A. Teigelhöfer, and F. Ames, Hyperfine Interact. **238**, 33 (2017).
[23] A. Teigelhöfer, P. Bricault, O. Chachkova, M. Gillner, J. Lassen, J. P. Lavoie, R. Li, J. Meissner, W. Neu, and K. Wendt, Hyperfine Interact. **196**, 161 (2010).
[24] R. Li, J. Lassen, S. Rothe, A. Teigelhöfer, and M. Mostamand, Opt. Express **25**, 1123 (2017).
[25] H. Heggen, Master thesis, Technische Universität Darmstadt, 2013.
[26] S. Raeder, H. Heggen, J. Lassen, F. Ames, D. Bishop, P. Bricault, P. Kunz, A. Mjøs, and A. Teigelhöfer, Rev. Sci. Instrum. **85**, 033309 (2014).
[27] A. Kramida, Yu. Ralchenko, J. Reader, and NIST ASD Team, NIST Atomic Spectra Database (ver. 5.7.1) [Online]. Available at https://physics.nist.gov/asd, National Institute of Standards and Technology, Gaithersburg, MD, 2019.
[28] U. Fano, C. E. Theodosiou, and J. L. Dehmer, Rev. Mod. Phys. **48**, 49 (1976).
[29] C. Morillon and J. Vergès, Phys. Scr. **12**, 129 (1975).
[30] S. Raeder, H. Heggen, A. Teigelhöfer, and J. Lassen, Spectrochim. Acta Part B **151**, 65 (2019).
[31] U. Fano, Phys. Rev. **124**, 1866 (1961).
[32] H. Hieronymus, J. Neukammer, and H. Rinneberg, J. Phys. B **25**, 3463 (1992).
[33] U. Fano and J. W. Cooper, Phys. Rev. **137**, A1364 (1965).
[34] W. E. Cooke, T. F. Gallagher, S. A. Edelstein, and R. M. Hill, Phys. Rev. Lett. **40**, 178 (1978).
[35] K. Afrousheha, Eur. Phys. J. Plus **129**, 25 (2014).
[36] S. T. Pratt, Phys. Rev. A **38**, 1270 (1988).
[37] D. A. Fink, K. Blaum, V. N. Fedosseev, B. A. Marsh, R. E. Rossel, and S. Rothe, Spectrochim. Acta Part B **151**, 72 (2019).